2010-01-0105
Published
04/12/2010

Hydrostatic Wheel Drives for Vehicle Stability Control

Sisay Molla, Justin Sill and Beshah Ayalew
International Center for Automotive Research, Clemson University

ABSTRACT

Hydrostatic (hydraulic hybrid) drives have demonstrated energy efficiency and emissions reduction benefits. This paper investigates the potential of an independent hydrostatic wheel drive system for implementing a traction-based vehicle lateral stability control system. The system allows an upper level vehicle stability controller to produce a desired corrective yaw moment via a differential distribution of torque to the independent wheel motors. In cornering maneuvers that require braking on any one wheel of the vehicle, the motors can be operated as pumps for re-generating energy into an on-board accumulator. This approach avoids or reduces activation of the friction brakes, thereby reducing energy waste as heat in the brake pads and offering potential savings in brake maintenance costs.

For this study, a model of a 4×4 hydrostatic independent wheel drive system is constructed in a causal and modular fashion and is coupled to a 7 DOF vehicle handling dynamics model. The integrated system model is then used to first verify component selection and hybrid control threshold settings for the independent drive system. Then, a vehicle stability controller is set up as a cascade of a yaw controller and a torque distribution strategy. The overall system is evaluated by simulating a reduced handling test maneuver. The energy recovery attributes of the independent drive system are clearly shown as changes in accumulator state of charge during the maneuver.

1. INTRODUCTION

Concerns about resource depletion and global warming have accelerated the exploration of alternative and energy efficient vehicle propulsion systems. One of these proposed alternatives are hydrostatic (hydraulic hybrid) drives, which have been shown to improve fuel efficiency over conventional drivetrains, particularly for urban vehicles characterized by frequent stop and go motion [1,2,3]. The high specific power (peak power per unit mass) of hydrostatic components opens up the possibility of using multiple but smaller pump/motors for a per-axle or per-wheel drive system.

On the other hand, vehicle stability control (VSC) systems help reduce accidents by minimizing driver's loss of control of the vehicle during emergency/aggressive maneuvers. Central to these VSC (also referred to as vehicle dynamics control (VDC)) systems is the generation of a corrective yaw moment on the vehicle through controlled proportioning of the longitudinal force on each tire of the vehicle. Most VSC systems available on the market today are brake-based and merely extend the functionality of mature hardware in ABS systems to affect the differential braking of individual wheels of the vehicle and generate the required corrective yaw moment [4,5,6]. However, this strategy could involve too much slow down of the vehicle against driver intent and lead to energy waste in the brakes and accelerated wear of brake-linings. The alternative approach for generating the corrective yaw moment for VSC is to distribute the tractive force between driving wheels and eliminate the listed drawbacks of brake-based VSC strategies [7,8,9,10]. Current solutions employing this strategy are the so-called torque-vectoring systems involving active differentials within conventional IC engine powertrains [11, 12].

In this paper, we study a solution where the traction force of each individual wheel can be controlled by modulating the torque output of the individual wheel motors[8,9,10]. The goal is to exploit the arrangement and integrate both the demonstrated energy efficiency benefits of hydraulic hybrids and the safety of vehicle stability control. We focus the discussion on a series hydraulic hybrid vehicle featuring independent wheel drives, but the VSC strategy can be implemented with similar independent wheel drives for series electric hybrids and pure electric and fuel cell vehicles.

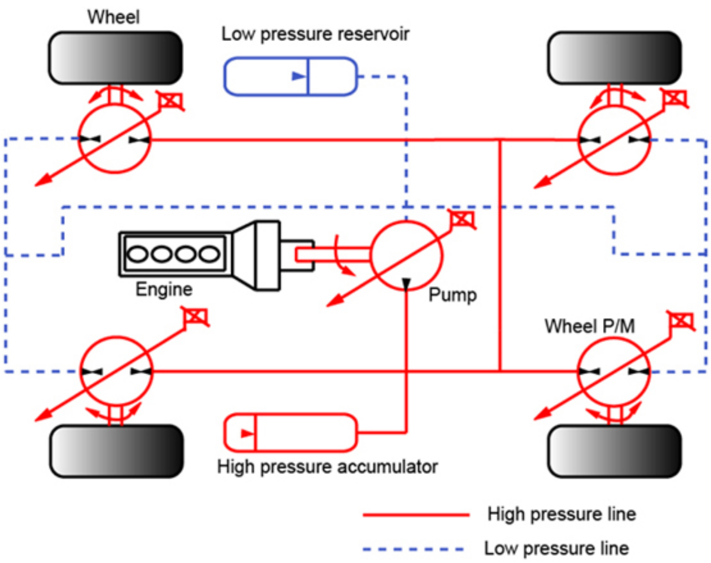

Figure 1. Schematic of a 4×4 Independent Hydrostatic Wheel Drive

Figure 1 shows the schematic of the proposed system. The engine (ICE) is directly connected to the pump. The fluid from the pump either charges the accumulator or directly flows to the individual wheel-end pump/motor (P/M). The ICE can be turned off when the vehicle comes to a full stop or when the SOC of the accumulator is greater than a minimum threshold value. The wheel-end P/M can be operated as a motor in drive mode or as a pump when regenerative braking is initiated and/or when the vehicle stability control dictates that it operate as a pump.

The rest of the paper is organized as follows. Section 2 details the system modeling adopted for the complete hydrostatic system as well as for the vehicle dynamics. Section 3 details the supervisory control strategies for powertrain performance and lateral stability control. Section 4 presents some results and discussions based on computer simulation of the developed models. Section 5 summarizes the conclusions of the work and highlights directions for further research.

2. SYSTEM MODELING

Figure 2 shows the high level system model architecture. It comprises of the subsystems of the engine and hydrostatic powertrain, the supervisory controller, the driver and vehicle dynamics models. The individual components of each of these subsystems are developed on the basis of forward-facing models interconnected by enforcing strict physical causality. The details of the component models are briefly outlined in the following subsections.

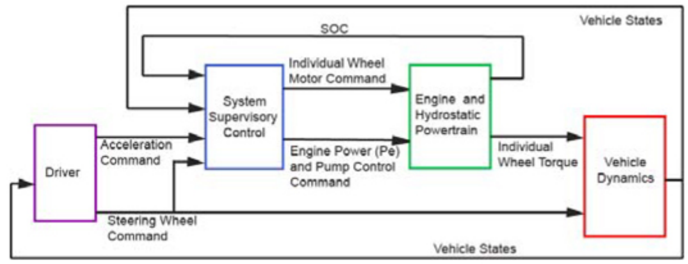

Figure 2. Schematics of high level system model

2.1. ENGINE AND HYDROSTATIC POWERTRAIN

Figure 3 shows the causal interconnection adopted for integrating the engine model, hydrostatic component models and the vehicle dynamics model.

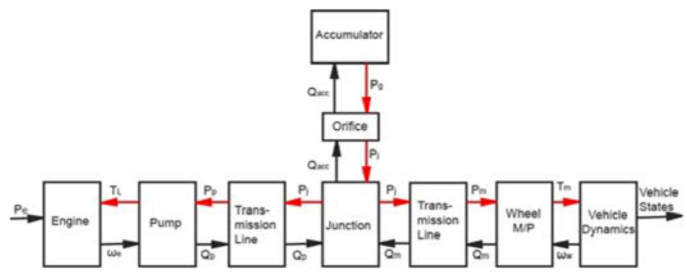

Figure 3. Input-output (Causality) relationships of hydrostatic powertrain component models

2.1.1. Engine Subsystem Model

The engine is implemented as a lookup table from the fuel consumption map of the engine and incorporating the dynamics of the engine/pump rotational inertia. The engine power (P_e) determined by the power management strategy in the supervisory controller and the minimum BSFC line of the engine intersect at a point on the engine torque-speed map which gives the desired engine torque T_e and desired engine speed ω_{e_des}. The engine output torque is considered to match the desired (i. e., torque generation delays are neglected). However, the actual speed of the engine/pump ($\omega_{e/p}$) is determined from the dynamics:

$$T_e - T_L = J_{eq.} * \dot{\omega}_{e/p} \tag{1}$$

where T_L is the load torque (pump torque) on the engine, and $J_{eq.}$ is of the engine/pump rotational inertia. The actual speed of the engine/pump from Eq. (1) is controlled via the displacement of the pump (through its displacement factor x defined below) to track the desired engine speed, ω_{e_des}. A PI controller is tuned to minimize the speed error.

2.1.2. Hydrostatic Powertrain Model

As shown in Figure 3, the hydrostatic powertrain connects the engine and the vehicle dynamics models.

Pump/Motor Model

The 4 pumps/motors (P/M) considered in this work are of the bent-axis design and are mechanically coupled to the wheels of the vehicle through a single gear ratio speed reduction unit. The P/M units convert available hydraulic power from the engine-mounted pump or the accumulator in to mechanical power for vehicle propulsion (motor mode), or convert the kinetic energy of the vehicle to hydraulic energy for storage in the accumulator (pump mode) during regenerative braking. Both the motor mode and pump mode can be activated for any one of the P/M units to generate a corrective yaw moment for vehicle stability control (VSC).

The P/M units (either at the engine or at the wheel-end) are modeled here as depicted in Figure 4. The main approach is to use a 3-D look up table using data from steady state measurements. The torque and the flow rate through the variable displacement P/M can be controlled by varying the displacement factor, x, which is defined as the ratio of the prevailing displacement to the maximum displacement of the machine. The causality of the model adopted is such that x, ω, and ΔP across the P/M are inputs and the volumetric efficiency η_v and the mechanical efficiency η_m of the P/M are interpolated for as outputs. Knowing the volumetric and mechanical efficiency values, the flow rate and the torque of the P/M can be computed by using the following sets of equations[13, 14]. First, the ideal flow rate of the P/M is given by:

$$Q_i = x\omega D \tag{2}$$

Then, the actual flow rate of the pump and the motor are calculated, respectively, by:

$$Q_{ap} = Q_i * \eta_v$$
$$Q_{am} = \frac{Q_i}{\eta_v} \tag{3}$$

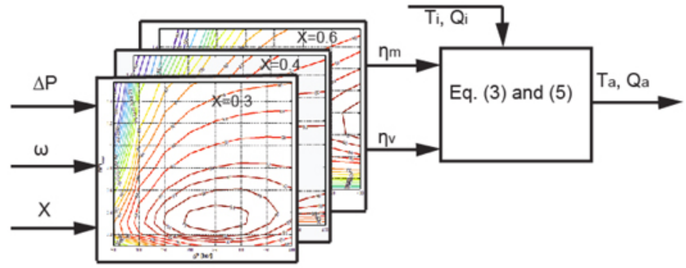

Figure 4. Steady-state lookup table based modeling of pumps and motors

Similarly, the ideal torque of the P/M is given by:

$$T_i = x\Delta PD \tag{4}$$

Then, the actual torque of the P/M is given by:

$$T_{ap} = \frac{T_i}{\eta_m}$$
$$T_{am} = T_i * \eta_m \tag{5}$$

The look up table approach we used here avoids the need for the numerous dimensionless numbers and loss coefficients frequently used in pump/motor modeling following the so called Wilson's pump theory[15, 16].

Accumulator/Reservoir Model

An accumulator is a pressure vessel that contains a hydraulic fluid and a pressurized gas (mostly nitrogen) where the two sides are separated by a bladder, a diaphragm or a piston. When hydraulic fluid is pumped in, the gas is compressed, resulting the pressure to increase and store energy. When the fluid is discharged through the P/M (in motor mode), the pressure in the gas decreases while delivering propulsion energy. A reservoir (or low pressure accumulator) is a hydraulic accumulator working at much lower pressure than the high pressure accumulator, but just enough to prevent the occurrence of cavitation in the pumps[3].

Detailed modeling of hydraulic accumulators has been undertaken earlier by Pourmovahed[14, 17]. Considering the use of elastomeric foam on the gas side of the accumulator (to reduce irreversible heat losses) and taking energy balance on the gas side, it can be shown that the temperature evolution is given by[14, 18]:

$$\left[1 + \frac{m_f c_f}{m_g c_v}\right]\frac{dT}{dt} = \frac{T_w - T}{\tau} - \frac{T}{C_v}\left(\frac{\partial p_g}{\partial T}\right)_v \frac{dv}{dt} \tag{6}$$

where τ is the thermal time constant and is defined as $\tau = m_g c_v / hA_w$. The pressure in the accumulator is related to the gas temperature and the specific volume through a real-gas equation of state. Here, we adopted the Beattie-Bridgeman (BB) equation of state given by[19]:

$$p_g = \frac{RT(1-\varepsilon)}{v^2} + (v+B) - A/v^2 \tag{7}$$

where,

$A = A_0(1 - a/v),\ B = B_0(1-b)/v,\ \varepsilon = c/(vT^3)$ and A_0, B_0, a, b, c are constants in the BB equation of state.

The sate of charge (SOC) of the accumulator is defined as the ratio of the instantaneous oil volume in the accumulator to the maximum oil capacity. However, measuring the instantaneous oil volume is not straightforward in a real-time application. As long as the temperature variation in the accumulator is kept low, the more directly measurable fluid/gas pressure can be used as an indicator of the SOC of the accumulator provided appropriate margins are considered [20].

Hydraulic Transmission Lines

The frequency of interest in the present study is rather low (a <10 Hz or so) that the dynamic effects of transmission lines are negligible compared to the dynamics of the other components. Therefore, a one dimensional lumped parameter resistive model, considering laminar or turbulent losses depending on the computed Reynolds number [14], is used for the transmission lines instead of more elaborate distributed parameter models [21].

2.1.2. Vehicle Dynamics Model Integration

The above hydrostatic powertrain model is integrated with a 7-DOF handling dynamics model [9, 10]. The model adopted includes the degrees of freedom of lateral, longitudinal and yaw motions of the vehicle body, as well as the rotations for each of the four tires. The schematic and equations for the adopted model are listed in the Appendix. Detailed derivations and discussions of the model are given in [9, 10, 22]. The tire/wheel dynamics connect the hydraulic wheel-end P/M torque to the dynamics of the vehicle via the longitudinal tire forces. The tire/wheel dynamics are given by:

$$I_w \dot{\omega}_i = T_{m,i} - F_{x,i} R_w \qquad \text{for } i = LF, RF, LR, RR \tag{8}$$

where LF, RF, LR and RR stand for left front, right front, left rear, and right rear tires. In the present study, since tractive forces are intended to influence the lateral dynamics, a proper tire model that considers combined slip conditions (longitudinal and lateral) must be used. However, tire data are often available as separate functions of the tire longitudinal slip ratio and normal load for longitudinal force (as $F_{x,\kappa} = F_x(\kappa, F_z)$) and the tire slip angle and normal load for the lateral force (for $F_{y,\alpha} = F_y(\alpha, F_z)$). The tire slip ratios and slip angles are computed from:

$$\kappa_i = \frac{\omega_i R_w}{V_{xi}} - 1 \qquad \text{for } i = LF, RF, LR, RR \tag{9}$$

$$\alpha_{LF} = \tan^{-1}\left(\frac{V_y + l_f \dot{\psi}}{V_x + \frac{T_f}{2}\dot{\psi}}\right) - \delta, \quad \text{and,} \quad \alpha_{LR} = \tan^{-1}\left(\frac{V_y - l_r \dot{\psi}}{V_x + \frac{T_r}{2}\dot{\psi}}\right) \tag{10}$$

where the RF, RR side slip angles are defined similarly (See the Appendix for definition of the variables). In this work, we considered the normal load changes that occur due to lateral and longitudinal accelerations as well as differences in the front and rear roll-stiffness distributions. The equations for updating the normal loads are given in the Appendix. The required combined slip model is arrived at by assuming that the contours of constant slip angle and constant slip ratio (in a F_y vs. F_x map) can be approximated by elliptical curves whose equations are given, respectively, by:

$$\left(\frac{F_x}{F_{x,\max}}\right)^2 + \left(\frac{F_y}{F_{y,\alpha}}\right)^2 = 1 \tag{11}$$

$$\left(\frac{F_x}{F_{x,\kappa}}\right)^2 + \left(\frac{F_y}{F_{y,\max}}\right)^2 = 1 \tag{12}$$

These are rather good approximations for actual tire data as can be seen in [23,24,25,26]. The set of ellipses for the constant slip angle contours (Eq.(11)) have a common point at the maximum longitudinal force. $F_{y,\alpha}$ is the lateral force for the pure lateral slip condition under a given slip angle. Therefore, when maximum longitudinal force is observed ($F_x = F_{x,max}$) there is no lateral force capacity. Conversely, the set of ellipses for the constant slip ratio contours (Eq.(12)) have a common value at the maximum lateral force, where $F_{x,\kappa}$ is the longitudinal force for the pure longitudinal slip condition under the given slip ratio. As F_y approaches $F_{y,max}$, the tire's longitudinal force capability reduces. Given the family of curves given by Eqs.(11) and (12), the combined tire forces for a given pair of slip angle and slip ratio can be found at the intersection of the ellipses. It can be shown that the combined slip longitudinal and lateral tire forces are given by:

$$F_x = F_{x,\kappa}\sqrt{\frac{(F_{x,\max}F_{y,\max})^2 - (F_{x,\max}F_{y,\alpha})^2}{(F_{x,\max}F_{y,\max})^2 - (F_{x,\kappa}F_{y,\alpha})^2}} \tag{13}$$

$$F_y = F_{y,\alpha}\sqrt{\frac{(F_{x,\max}F_{y,\max})^2 - (F_{x,\kappa}F_{y,\max})^2}{(F_{x,\max}F_{y,\max})^2 - (F_{x,\kappa}F_{y,\alpha})^2}} \tag{14}$$

This novel approach of synthesizing forces for the combined slip conditions forces allows the use of tire data mostly available for pure slip conditions (pure longitudinal slip and pure lateral slip) in our vehicle dynamics model. Note that combined slip considerations are central to the workings of the traction-based stability control addressed here. However, we state that the above model, while expedient, has limitations in replicating experimental data at high slip ratios and slip angles typically beyond tire-saturation levels.

3. SUPERVISORY CONTROL

The supervisory controller is the top level control where the command for engine power, the individual wheel torque commands (via the displacement factors), and supplementary friction brake activation command are determined to meet the vehicle safety and energy efficiency objectives. As shown in Figure 2, the supervisory controller takes the vehicle state (lateral acceleration, longitudinal speed, yaw rate, and rotational speed of individual wheels), driver steering wheel and acceleration, and the SOC of the accumulator as input commands from the sub-models of vehicle dynamics, driver and hydrostatic powertrain, respectively, and determines the individual wheel torque, the engine power and friction brake activation commands for the hydrostatic, and vehicle dynamics sub models.

3.1. POWER MANAGEMENT STRATEGY

A power management strategy is needed to determine the split between the two power sources (Engine/pump or accumulator) in such a way as to minimize the fuel consumption and reduce pollutant emissions. Different energy management strategies have been discussed in the literature on hybrid vehicles [3, 13, 20, 27,28,29]. In the present work a robust, albeit simple management strategy described in [20] is implemented. In this strategy, the engine power command (P_e) increases or decreases progressively based on the SOC of the accumulator. As long as the SOC is above the threshold value, say 0.4 (or 40%), the engine power command is zero. When the SOC of the accumulator drops below the threshold value, the engine starts charging the accumulator with a pre-determined threshold power command (say 45 kW). A dead band of 0.1 (10%) or so is taken to alleviate frequent engine on-off cycling. If the power demand for propulsion exceeds the threshold command, the SOC will drop below the lower limit of the dead band (i. e, 30%) and the engine power command is then progressively increased along the minimum BSFC line on the torque-speed map of the engine. Further increase in demand keeps the powertrain to work in a hydrostatic continuously variable transmission (CVT) mode and makes sure that the lower value of the SOC of the accumulator is kept above a minimum value. Further details of the strategy can be found in [20].

The other function of supervisory control is the activation of supplementary friction brakes. If the vehicle needs to decelerate further while the SOC of the accumulator indicates full (accumulator reaches maximum pressure) or if the torque available from the hydraulic system is not enough for braking, then the friction brakes need to be activated to bring the vehicle to the desired speed.

3.2. VEHICLE STABILITY CONTROL

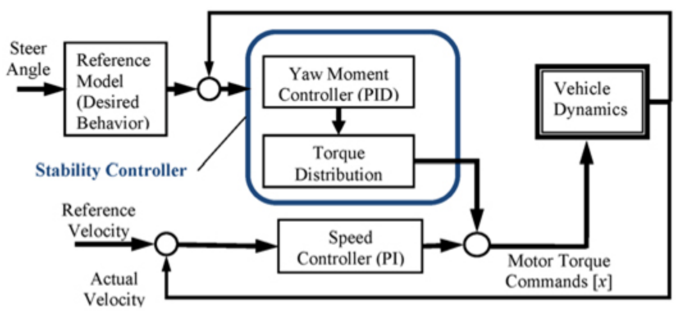

Figure5. Schematic of vehicle stability controller architecture

The stability control system modulates the torque of the wheel P/M in driving or braking to positively alter the vehicle attitude and trajectory without degrading the driver's intentions. This is achieved through a cascade of yaw moment control and a torque distribution strategy as seen in Figure 5. Several yaw moment controllers (yaw rate feedback, lateral acceleration feedback or combined feedback), and torque distribution strategies have been previously assessed for some strengths and weaknesses [9, 10], though an ideal strategy has yet to be conclusively determined. In this paper, a simple 2 DOF steady-state handling response model is used to define a desired vehicle behavior based on vehicle velocity and driver steering input. We also restrict the discussion to a yaw rate feedback stability controller (of a PID type), which compares the desired yaw rate to the actual yaw rate of the vehicle to determine if the vehicle has excessive or insufficient yaw rate (over-steer or under-steer). If excessive yaw rate error is observed, the stability controller acts to reduce the yaw rate error by applying a corrective yaw moment. The torque distribution strategy then dictates how the corrective yaw moment is achieved by modulating the torque output of the individual wheel-end P/M via the displacement factor *x*. The distribution strategy applied in this work (form a total of 4 suggested in previous work [9]) involves reducing the torque of the wheel P/Ms on the left or right sides of the vehicle to generate a positive or negative yaw moment.

4. RESULTS AND DISCUSSION

4.1. COMPONENT SELECTION AND OPTIMIZATION

The system model described in Section 2 along with the power management strategy described Section 3.1 was used to select component sizes and control threshold parameters for the independent hydrostatic drive system proposed in Figure 1, with the objective of improving fuel mileage and acceleration performance for a mid-size truck. We started with the stock engine for a Ford F-150 truck (4.5 L, V-8, 172kW SI engine) and considered the upgraded powertrain with the independent hydrostatic drive to work with as a larger truck with a GVW of 8000 lbs (about 20% heavier). In addition, we limited the selection of the hydrostatic components to stock components for which test data were available. The following components are the result of the iterative optimization and component selection exercise: wheel-end P/M displacement of 55 cm^3/rev; engine mounted pump displacement of 125 cm^3/rev; gear ratio between the P/M and the wheel of 4.00; and accumulator volume of 20 gallon. Using these sets of component sizes, further fuel economy optimization and safety considerations led to the following sets of parameters for the accumulator and engine operating thresholds: Pre-charge pressure =13 MPa, Maximum pressure = 40 MPa, engine-off SOC threshold SOC = 40%, SOC dead band = 10%, threshold engine power=45 kW (engine power in dead band).

4.2. LONGITUDINAL PERFORMANCE

Figure 6 shows some of the responses of the system for the first 400 seconds of the FUDS drive cycle. Figure 6a shows the SOC and vehicle speed response history and Figure 6b shows the engine and accumulator power. For the first 25 seconds, the engine power is zero as the SOC is greater than the threshold. At 20 seconds, the vehicle starts to accelerate with the accumulator discharging (negative accumulator power), but after 25 seconds up to around 120 sec the engine was turning on and off keeping the SOC fluctuation between 30% and 40% (dead band). The first substantial braking event starting at the 125th second charges the accumulator to around 70% and the engine is turned off. When the vehicle accelerates rapidly (190-205 sec), the SOC of the accumulator drops below the minimum threshold value and therefore, the engine power increases progressively to overcome the increased power demanded by the vehicle and recharge the accumulator.

A cursory look at the fuel economy results in Table 1 indicates the expected significant benefits from the hybridization, particularly in city driving. We also included results for a 2-motor front wheel drive (FWD) to point out that the 2-motor drives does improve the fuel economy further. This can be explained by the fact that when the vehicle is propelled by 2 motors, each of the motors takes up larger loads than the case with 4-motors (4WD) as shown in Figure 6c. Higher load is favorable for hydraulic machines as the efficiency of each machine increases. However, the acceleration performance suffers when using 2-motors. Furthermore, 2-motor propulsion reduces the choice of P/Ms that can act as actuators for implementing vehicle stability control.

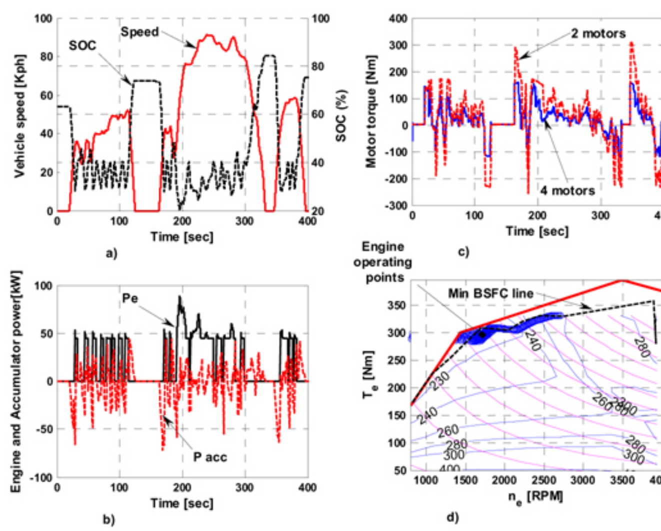

Figure 6. System responses for the first 400 sec of FUDS a) vehicle speed and accumulator SOC, b) Engine power (P_e) and accumulator power(P_{Acc}), c) Wheel P/M torques for 2-motor and 4-motor independent drives, d) Engine operating points on its torque-speed map

<table 1 here>

Table 1. Fuel economy improvements with independent hydrostatic wheel drive over the conventional truck.

	Conventional Truck,. Ford F150, 4WD, V8, 4.6L, Automatic 4spd [US DOE, fueleconomy.gov] (MPG)	Independent Hydrostatic Wheel Drive (4 Motors, 4WD) (% improvements)	Independent Hydrostatic Wheel Drive (2Motors, FWD) (% improvement)
City Cycle (FUDS)	14	36	56
Highway Cycle (HWFET)	18	10	25

4.3. LATERAL STABILITY

The complete system model described in Section 2 is laterally exercised, along with the stability controller described in Section 3.2, at a target forward speed of 80 kph with a "sine with dwell" steering angle input defined by NHTSA to emulate a severe avoidance maneuver [30]. The responses with and without the stability controller are shown in Figure 7 for a vehicle with font-rear distributions of 55-45 in weight, 55-45 in drive and 30-70 in roll stiffness, and on dry asphalt road.

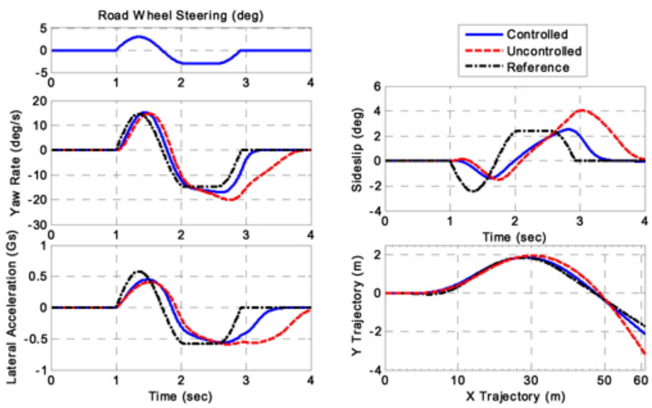

Figure 7. Controlled and uncontrolled vehicle performance

The reference model used here has no inertia dynamics (just 2 DOF steady-sate gains) and is based only on driver steering angle input and vehicle velocity. Therefore, the actual vehicle responses exhibit a delay in responding to the driver's steering input (controlled or uncontrolled). Still, the vehicle response with the stability controller shows significant improvement as compared to the uncontrolled response. No excessive side slip angles and yaw rates are exhibited with the stability controlled vehicle with the proposed system.

Furthermore, the stability controller uses entirely the wheel-end P/M to accomplish the course corrections with out using the friction brakes. Figure 8 below shows the performance of the hydrostatic powertrain during the same avoidance maneuver considered in Figure 7. Unlike a traditional brake-based VSC system where energy is wasted as heat while accomplishing the corrections, this independent hydrostatic drive VSC system can recover some of the energy (while generating the yaw moment) by momentarily recharging the accumulator. Note that for this particular maneuver, the engine is turned off just before the start of the steer maneuver (top left plot). The SOC of the accumulator goes up momentarily (positive charging power) when the left wheel P/M and then the right wheel P/M are operated as pumps. Eventually, as the priority energy source (with SOC higher than the threshold of 30% defined in the power management strategy), the accumulator provides the bulk of the propulsion power for the rest of the maneuver (without the engine turning on), until shortly after the vehicle has returned to the straight ahead portion. This results show the potential of independent hydrostatic wheel drives for integrating regenerative braking for energy efficiency, and torque distribution for vehicle stability control.

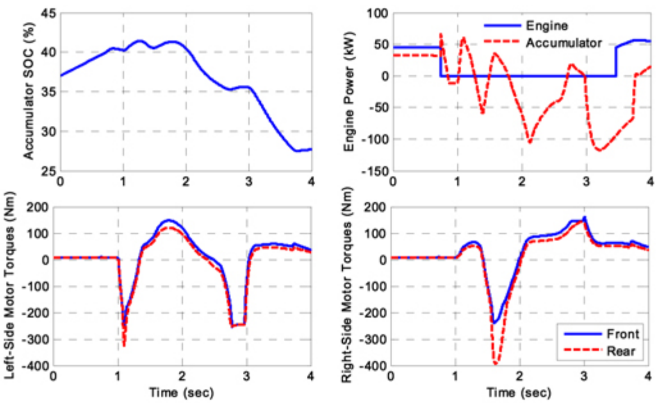

Figure 8. Performance of the hydrostatic powertrain during the stability controlled maneuver

5. CONCLUSIONS AND FUTURE WORK

In this paper, an independent hydrostatic wheel drive system has been considered from the point of view of enabling vehicle dynamics control function in addition to fuel consumption minimization. A detail causal forward-facing model of the proposed system has been outlined, including those of the hydrostatic system components (pump, wheel-end pump/motors, accumulators and transmission lines), the engine and the 7 DOF vehicle dynamics. A simplified combined tire-slip model suitable for the traction-based stability control has been derived and implemented. A power management strategy forms the first layer of supervisory control which uses the accumulator state of charge to determine the allocation of power demand to the two-onboard sources and allow the engine to operate along its minimal BSFC line. Another layer of the supervisory control deals with vehicle dynamics stability control, wherein a corrective yaw moment is determined based on yaw rate feedback error and then a torque distribution strategy allocates the torque demand to each wheel-end motor to generate the required corrective yaw moment.

The system model was used to analyze the performance of a mid-size truck, which was about 20% heavier than the baseline truck to take into account the upgraded capability and weight from the added hydrostatic system components. The results show the expected fuel economy benefits of over 36% on the FUDS (city cycle) and over 10% on the HWFET (highway cycle), with even further saving noted with a 2-

motor drive instead of 4-motor drive. Furthermore, exercising the system model for a typical avoidance maneuver ("sine with dwell" test) showed how vehicle stability control schemes implemented with the independent hydrostatic drive system can include energy regeneration events within handling maneuvers. The proposed independent drive systems can effectively integrate energy efficiency and vehicle safety functions. Further maintenance cost savings are enabled from minimizing friction brakes.

Further work on this topic will include: the improvement of the vehicle dynamics model to incorporate dynamic suspension effects (roll, pitch, heave), improvement of combined tire-slip model to handle tire saturation, investigation of alternative yaw moment controllers (estimated side-slip angle and lateral acceleration feedback) and torque distribution strategies (progressive engagement based on degree of instability or weight transfer), and implementation of alternative power management strategies. Finally, work is already in progress at the Clemson University-International Center for Automotive Research, to demonstrate the proposed system with a hardware-in-the loop test setup.

6. REFERENCES

1. Kargul, John J. Hydraulic Hyrbids: Cost-Effective Clean Urban Vehicles. in *Michigan Clean Fleet Conference*. March 22, 2006 2006, Detroit, MI.

2. Buchwald, P., Christensen, G., Larsen, H., and Pedersen, P. S., "Improvement of a Citybus Fuel Economy Using a Hydraulic Hybrid Propulsion System- A Theoretical and Experimental Study,". SAE Technical Paper 790305, 1979.

3. Wu, Bin, Lin, Chan-Chiao, Filipi, Zoran, Peng, Huei, and Assanis, Dennis. Optimal Power Management for a Hydraulic Hybrid Delivery Truck. *Vehicle System Dynamics*. 2004. 42(1/2): p. 23-40.

4. van Zanten, A.T., "Bosch ESP Systems: 5 Years of Experience," SAE Technical Paper 2000-01-1633, 2000.

5. Ghoneim, Youssef, Lin, William, Sidlosky, David, Chen, Hsien, Chin, Yuen-Kwok, and Tedrake, Michael. Integrated Chassis Control System to Enhance Vehicle Stability. *International Journal of Vehicle Design*. 2000. 23(1/2): p. 124-144.

6. Rajamani, Rajesh. Vehicle Dynamics and Control. 2006. Springer.

7. Esmailzadeh, E, Goodarzi, A, and Vossoughi, G R. Directional Stability and Control of Four-Wheel Independent Drive Electric Vehicles. *Proc Instn Mech Engrs Part K: J Multi-body Dynamics*. 2002. Vol 216(4): p. 303-313.

8. Goodarzi, Avesta and Esmailzadeh, Ebrahim. Design of a VDC System for All-Wheel Independent Drive Vehicles. *IEEE/ASME Transactions on Mechatronics*. 2007. 12(6): p. 632-639.

9. Karogal, I. and Ayalew, B., "Independent Torque Distribution Strategies for Vehicle Stability Control," SAE Technical Paper 2009-01-0456, 2009.

10. Osborn, R.P. and Shim, T., "Independent Control of All-Wheel-Drive Torque Distribution," SAE Technical Paper 2004-01-2052, 2004.

11. Piyabongkarn Damrongrit, Lew Jae Y., Rajamani Rajesh, Grogg John A., and Yuan, Qinghui. On the Use of Torque-Biasing Systems for Electronic Stability Control: Limitations and Possibilities. *IEEE Transaction on Control Systems Technology*. 2007. 15(3): p. 581-589.

12. Gradu, M., "Torque Bias Coupling for AWD Applications," SAE Technical Paper 2003-01-0676, 2003.

13. Filipi, Z., Louca, L., Daran, B., Lin, C-V., Yildri, U., Wu., B., Kokkolaras, M., Assanis, D., Peng, H., Papalambros, P., Stein, J., Szukubiel, D., and Chapp, R. Combined Optimization of Design and Power Management of the Hydraulic Hybrid Propulsion System for the 6×6 Medium Truck. *Int. J. of Heavy Vehicle Systems*. 2004. 11(3/4): p. 372-402.

14. Pourmovahed, A., Beachley, N.H., and Fronczak, F.J. Modeling of a Hydraulic Energy Regeneration System- Part I: Analytical Treatment. *Transactions of ASME, Journal of Dynamic Systems, Measurement and Control*. 1992. 114: p. 155-159.

15. McCandlish, D. and Dorey, R. E. The Mathematical Modeling of Hydrostatic Pumps and Motors. *Proceeding of Inst. Mech. Engineers. Part B.*. 1984. 198(10): p. 165-174.

16. Wilson, W. E. Rotary-Pump Theory. *ASME Transactions*. 1946. 68(4): p. 371-384.

17. Pourmovahed, A., Beachley, N. H., and Fronczak, F. J. Modeling of a Hydraulic Energy Regeneration System- Part Ii: Experimental Program. *Transactions of ASME, Journal of Dynamic Systems, Measurement and Control*. 1992. 114: p. 160-165.

18. Pourmovahed, A. An Experimental Thermal Time Constant Correlation for Hydraulic Accumulators. *Transactions of ASME, Journal of Dynamic Systems, Measurement and Control*. 1990. 112: p. 116-121.

19. Cengel, Yunus A. and Boles, Michael A. Thermodynamics: An Engineering Approach, 5th Edition. 2005. McGraw Hill.

20. Kim, Y.J. and Filipi, Z., "Simulation Study of a Series Hydraulic Hybrid Propulsion System for a Light Truck," SAE Technical Paper 2007-01-4151, 2007.

21. Watton, John. Fluid Power Systams: Modeling, Simulation, Analog and Microcomputer Control. 1989. Prentice Hall International(UK) LTD.

22. Genta, Giancarlo. Motor Vehicle Dynamics: Modeling and Simulation. Series on Advances in Mathematics for

Applied Sciences. Vol. 43. 1997. Singapore. World Scientific Publishing.
23. Svendenius, J. and Gafvert, M., “A Brush-Model Based Semi-Empirical Tire-Model for Combined Slips,” SAE Technical Paper 2004-01-1064, 2004.
24. Brach, R.M. and Brach, R.M., “Modeling Combined Braking and Steering Tire Forces,” SAE Technical Paper 2000-01-0357, 2000.
25. Pottinger, M.G., Pelz, W., and Falciola, G., “Effectiveness of the Slip Circle, “COMBINATOR”, Model for Combined Tire Cornering and Braking Forces When Applied to a Range of Tires,” SAE Technical Paper 982747, 1998.
26. Pacejka, Hans. Tyre and Vehicle Dynamics. 2002. Oxford: Butterworth-Heinemann.
27. Jalil, Nashat, A.Kheir, Naim, and Salman, Mustasim. A Ruled-Based Energy Management Strategy for a Series Hybrid Vehicle in *Proceeding of the American Control Conference* June 4-6 1997. 1, Albuquerque, NM.
28. BrahmaA., GuezennrcY., and RizzoniG.. Optimal Energy Mangement in Series Hybrid Electric Vehicles. *proceedings of the American Control Conference* 2000: p. 60-64.
29. Musardo, Cristian, Rizzoni, Giorgio, and Staccia, Benedetto. A-ECMS: An Adaptive Algorithm for Hybrid Electric Vehicle Energy Management. in *Proceeding of the 44th IEEE Conference on Decision and Control and the European Control Conference*. December 12-15 2005.
30. NHTSA. FMVSS-126; Electronic Stability Control Systems; Controls and Displays, US Department of Transportation. 2007.

7. CONTACT INFORMATION

Dr. Beshah Ayalew
Clemson University-International Center for Automotive Research
4 Research Dr.
Room 342 CGEC
Greenville, SC 29650, USA
beshah@clemson.edu
Phone: 864-283-7228.

8. NOMENCLATURE/ABREVIATIONS

A
: vehicle frontal area

A_w
: effective accumulator wall area

BSFC
: basic specific fuel consumption

C_D
: drag coefficient

c_f
: constant pressure specific heat of foam

c_v
: constant volume specific heat of gas

D
: maximum displacement of pump/motor

F_x
: longitudinal tire force

$F_{x, max}$
: maximum longitudinal tire force

$F_{x, \kappa}$
: longitudinal tire force at slip ratio κ

F_y
: lateral tire force

$F_{y, max}$
: maximum lateral tire force

$F_{y,\alpha}$
: lateral for tire force at given slip angle α

F_z
: normal tire load

g
: gvitational constant

h
: heat transfer coefficient

h_{cg}
: vehicle C.G. height

h_{rcF}
: front roll center height

h_{rcR}
rear roll center height

I_{zz}
yaw inertia

I_{w}
inertia of motor/wheel referred to wheel

J_{eq}
equivalent inertia of the pump/engine

$K_{\phi R}$
rear roll stiffness

$K_{\phi L}$
front roll stiffness

l
wheel base

l_f
distance of front axle from vehicle C.G.

l_r
distance of rear axle from vehicle C.G.

m
total vehicle mass

m_f
mass of the foam

m_g
mass of the gas in accumulator

P_e
engine power

p_g
gas pressure

p_j
junction pressure

p_p
pump pressure

p_m
motor pressure

Q_{acc}
accumulator flow rate

Q_{ap}
actual pump flow rate

Q_{am}
actual motor flow rate

Q_i
ideal flow rate

R_{w}
effective wheel radius

t
time

T_{ap}
actual pump torque

T_{am}
actual motor torque

T_f
front wheel track width

T_r
rear wheel track width

T_{i}
ideal torque

T_L
load torque

T_w
accumulator wall temperature

$\boldsymbol{V_x}$
longitudinal velocity in vehicle x-axis

$\boldsymbol{V_y}$
lateral velocity in vehicle y-axis

$\boldsymbol{v}$
specific volume of the gas

$\boldsymbol{x}$
displacement factor for pump/motor

$\boldsymbol{\omega_{e\_des}}$
desire rotational speed of the engine

$\boldsymbol{\omega_i}$**, or,** $\boldsymbol{\omega_w}$
rotational speed of wheel *i*

$\boldsymbol{\omega_{e/p}}$
actual rotational speed of the engine/pump

$\boldsymbol{\alpha_i}$
lateral slip angle of tire *i*

$\boldsymbol{\delta}$
road steering wheel angle

$\boldsymbol{\rho}$
density of air

$\boldsymbol{\kappa_i}$
longitudinal slip of tire *i*

$\dot{\psi}$
vehicle yaw rate

$\boldsymbol{\tau}$
thermal time constant

$\boldsymbol{\eta_v}$
volumetric efficiency

$\boldsymbol{\eta_m}$
mechanical efficiency

$\boldsymbol{\Delta P}$
pressure difference across pump/moto[SM1]r

APPENDIX

Please see the definitions above for the notations and Figure A1 below for the schematic of the model adopted. The longitudinal, lateral, and yaw equations are:

$$m\left(\dot{V}_y + V_x\dot{\psi}\right) = \sum F_y = \left(F_{yLF} + F_{yRF}\right)\cos(\delta) + F_{yLR} + F_{yRR} + \left(F_{xLF} + F_{xRF}\right)\sin(\delta) \quad (A1)$$

$$m\left(\dot{V}_y + V_x\dot{\psi}\right) = \sum F_y = \left(F_{yLF} + F_{yRF}\right)\cos(\delta) + F_{yLR} + F_{yRR} + \left(F_{xLF} + F_{xRF}\right)\sin(\delta) \quad (A2)$$

$$\begin{aligned} I_{zz}\ddot{\psi} = \sum M_z = l_f\left[\left(F_{yLF} + F_{yRF}\right)\cos(\delta) + \left(F_{xRF} + F_{xLF}\right)\sin(\delta)\right] + l_r\left(F_{yLR} + F_{yRR}\right) \\ + \frac{T_f}{2}\left[\left(F_{xRF} - F_{xLF}\right)\cos(\delta) + \left(F_{yLF} - F_{yRF}\right)\sin(\delta)\right] + \frac{T_r}{2}\left(F_{xRR} - F_{xLR}\right) \end{aligned} \quad (A3)$$

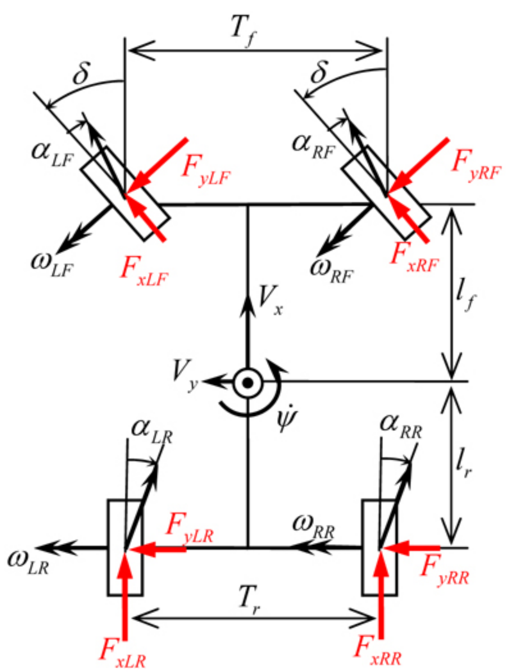

Figure A1. Schematic of Vehicle Dynamics Model

The normal loads on the LF and LR tires (the others follow similarly) are given by:

$$\begin{aligned} F_{LF} &= \frac{mgl_r}{2L} - \left(\dot{V}_y + V_x\dot{\psi}\right)\left(\frac{ml_r h_{rcF}}{LT_f} + \frac{m\left(h_{cg} - h_{rcF}\right)K_{\phi F}}{T_f\left(K_{\phi F} + K_{\phi R} - mg\left(h_{cg} - h_{rcF}\right)\right)}\right) - \left(\dot{V}_x - V_y\dot{\psi}\right)\left(\frac{mh_{cg}}{2L}\right) \\ F_{LR} &= \frac{mgl_f}{2L} - \left(\dot{V}_y + V_x\dot{\psi}\right)\left(\frac{ml_f h_{rcR}}{LT_r} + \frac{m\left(h_{cg} - h_{rcR}\right)K_{\phi R}}{T_r\left(K_{\phi F} + K_{\phi R} - mg\left(h_{cg} - h_{rcR}\right)\right)}\right) + \left(\dot{V}_x - V_y\dot{\psi}\right)\left(\frac{mh_{cg}}{2L}\right) \end{aligned} \quad (A4)$$